

# Nanocrystalline intermetallics on mesoporous carbon for direct formic acid fuel cell anodes

Xiulei Ji<sup>1</sup>, Kyu Tae Lee<sup>1</sup>, Reanne Holden<sup>1</sup>, Lei Zhang<sup>2</sup>, JiuJun Zhang<sup>2</sup>, Gianluigi A. Botton<sup>3</sup>, Martin Couillard<sup>3</sup> and Linda F. Nazar<sup>1\*</sup>

**Shape- and size-controlled supported metal and intermetallic nanocrystallites are of increasing interest because of their catalytic and electrocatalytic properties. In particular, intermetallics PtX (X = Bi, Pb, Pd, Ru) are very attractive because of their high activity as fuel-cell anode catalysts for formic acid or methanol oxidation. These are normally synthesized using high-temperature techniques, but rigorous size control is very challenging. Even low-temperature techniques typically produce nanoparticles with dimensions much greater than the optimum <6 nm required for fuel cell catalysis. Here, we present a simple and robust, chemically controlled process for synthesizing size-controlled noble metal or bimetallic nanocrystallites embedded within the porous structure of ordered mesoporous carbon (OMC). By using surface-modified ordered mesoporous carbon to trap the metal precursors, nanocrystallites are formed with monodisperse sizes as low as 1.5 nm, which can be tuned up to ~3.5 nm. To the best of our knowledge, 3-nm ordered mesoporous carbon-supported PtBi nanoparticles exhibit the highest mass activity for formic acid oxidation reported to date, and over double that of Pt-Au.**

Much attention has recently been focused on low-temperature fuel cells with energy conversion based on formic acid (HCOOH) instead of methanol<sup>1,2</sup>, because HCOOH exhibits much lower crossover flux through Nafion membranes<sup>3</sup>. However, such cells require a bimetallic catalyst at the anode (fuel) side, because conventional catalysts such as platinum are readily self-poisoned by the CO that is produced as a side product<sup>4,5</sup>. This is explained by the 'dual-path reaction mechanism'<sup>6-8</sup>. In the desirable path, sequential dehydrogenation steps lead to the direct formation of CO<sub>2</sub> from formic acid (path 1). In the undesirable path, CO, formed as a reaction intermediate via dehydration (path 2), readily adsorbs onto the platinum surface, and impedes further fuel oxidation. It is widely believed that the dehydration path requires the presence of platinum atom ensembles—continuous neighbouring atomic sites—whereas the dehydrogenation path does not<sup>9</sup>. This explains the poor properties of platinum metal. Furthermore, the CO poisoning effect can be inhibited by the breach of platinum ensembles. By using bulk platinum with adatoms on the surface<sup>10-14</sup> or bulk PtM (M: Bi, Pb, Pd) intermetallic catalysts<sup>15-17</sup>, resistance to CO poisoning of the catalysed formic acid oxidation is improved.

Catalyst composition is not the only important factor. To prepare an efficient gas diffusion electrode, the catalyst particles must have nanoscale dimensions, are ideally monodisperse, and should be supported on porous carbon. Nanoparticles are necessary to achieve high mass activity and complete resistance to CO poisoning. Literature reports cite difficulty in synthesizing intermetallics in nanocrystalline form at low temperatures where sintering does not result in particle aggregation, although some progress has been achieved. By applying the polyol process<sup>18</sup> or a co-reduction method using sodium borohydride<sup>19,20</sup>, DiSalvo, Abruña and colleagues generated unsupported intermetallic PtBi and PtPb nanoparticles (~20 nm or larger). Although the mass activity of these catalysts was not maximized due to particle

agglomeration, nearly complete elimination of CO poisoning was observed. Special synthetic procedures are required to avoid agglomeration of the alloy nanoparticles that are normally formed at high temperatures.

Recently, new advances in particle size control of supported intermetallic materials have been reported. Schaak and colleagues introduced the preparation of supported intermetallic nanocrystals, including PtBi, by using pre-formed supported single metal nanoparticles as nucleation sites<sup>21</sup>. However, upon annealing to nucleate intermetallic phases, these unconfined metal particles typically grow larger than desired. To date, major efforts have been devoted to particle size control of intermetallic nanoparticles, with only limited success. Another difficulty is in preparing the catalysts directly supported on carbon, while simultaneously achieving good crystallite size control. It is well known that the performance of a catalyst layer in a fuel cell is influenced by where and how these particles are supported<sup>22</sup>. A good catalyst support should be efficient in charge and mass transfer, and capable of inhibiting sintering and loss of the catalyst during operation. Improvements in the development of supported catalysts based on intermetallics requires a reliable methodology that facilitates not only particle size control but the fine dispersion of these nanoparticles on a support such as ordered mesoporous carbon (OMC)<sup>23</sup>.

OMCs have many desirable characteristics, including interconnected porous structures, narrow pore size distributions and high surface areas, and have attracted much attention for their application as catalyst supports for fuel cells<sup>24-27</sup>. To maximize the mass activity of a catalyst and take advantage of the unique architectures of the OMC, it is vital that the catalyst nanoparticles be loaded within the mesoporous voids. This has proven very challenging. The so-called 'wet' process—the only route explored to date<sup>24,28</sup>—is limited by the poor compatibility between the hydrophobic carbon and the hydrophilic solvents necessary to dissolve the

<sup>1</sup>University of Waterloo, Department of Chemistry, Waterloo, Ontario, Canada N2L 3G1, <sup>2</sup>Institute for Fuel Cell Innovation, National Research Council Canada, Vancouver, British Columbia, Canada V6T 1W5, <sup>3</sup>McMaster University, Department of Materials Science and Engineering, Hamilton, Ontario, Canada L8S 4L8. \*e-mail: lfnazar@uwaterloo.ca

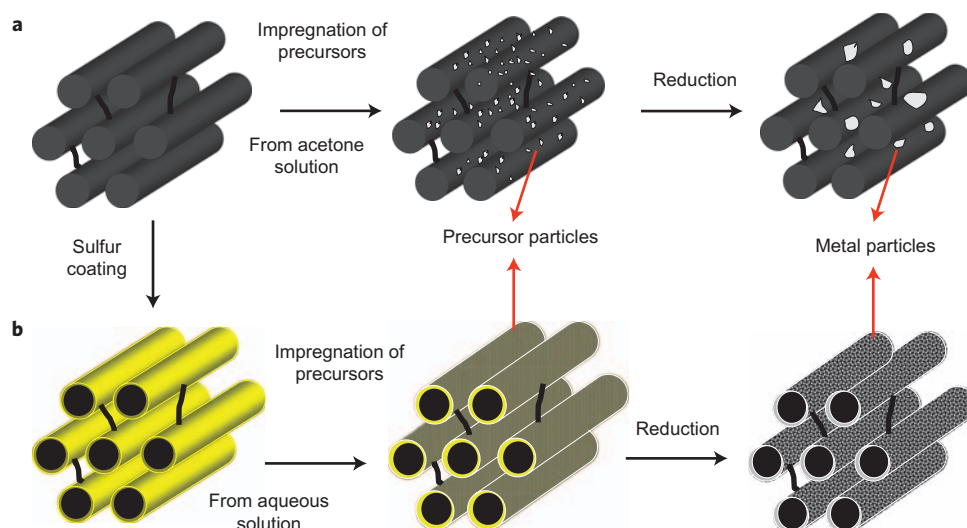


**Figure 1** | Schematic illustrating the nucleated-growth synthesis of OMC-supported noble metal and intermetallic nanocrystallites. **a**, The conventional impregnation method used to load noble metal nanoparticles into OMC. **b**, The present impregnation method, using sulfur-functionalized OMC to act as a metal trap to nucleate noble metals (Pt, Pd, Ru, Rh) or intermetallics (PtBi).

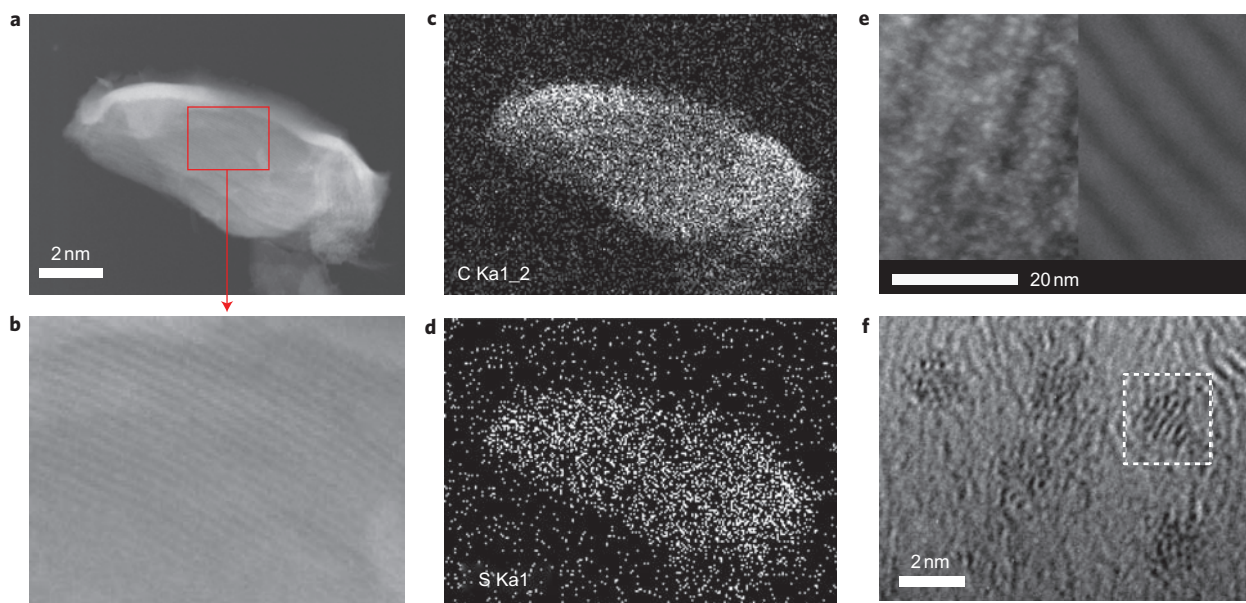


**Figure 2** | TEM images demonstrating the formation of OMC-supported platinum nanocrystallites with dimensions of  $<2$  nm. **a**, STEM overview of OMC-S. **b**, Image expansion corresponding to the area outlined by the red square in **a**. **c,d**, Corresponding carbon and sulfur elemental maps using EDX. **e**, Dark-field composite image comparing OMC-Pt-1.5 nm (left) and pristine OMC (right). **f**, Bright-field HRTEM image of OMC-Pt-1.5 nm.

catalyst precursors. This results in heterogeneous particle size distribution both within and on the outer surface of the OMC. To solve this problem, one approach is to transform the OMC into a more hydrophilic material<sup>29,30</sup>. However, successful modification of OMCs that facilitates metal nanoparticle loading has not been reported<sup>31</sup>. As an alternative approach, one-pot synthesis of platinum-based nanoparticles has recently been investigated<sup>32–36</sup>. Typically, these nanoparticles are embedded within the walls of mesoporous structures. They show improved methanol tolerance as cathode catalysts for direct methanol fuel cells, but suffer from poor accessibility of the catalysts. Here, we introduce a highly reliable synthetic strategy that enables a wide range of noble metal or intermetallic nanoparticles to be encapsulated within the OMC voids, resulting in ultrafine dispersion and narrow particle size distribution while giving free access to the catalyst centres. The

encapsulated intermetallic PtBi shows excellent catalytic performance in formic acid oxidation.

## Results and discussion

Our proof-of-concept studies are based on CMK-3, a well investigated OMC<sup>37</sup>, as illustrated in Fig. 1. In a departure from any previously reported approaches, we modified the carbon surface with sulfur (OMC-S), which functions as a metal trap. Normally considered to be a potent catalyst poison, sulfur exhibits a strong affinity for noble metals owing to a soft acid–soft base interaction<sup>38,39</sup>. A thin layer of sulfur on OMC is used as a mediator that acts to absorb and bind the catalyst metal precursors from solution into the OMC, and additionally restricts their particle growth during reduction to result in ultrafine dispersions of metal nanocrystallites. The sulfur is readily imbibed by capillary forces into the OMC

framework from a sulfur melt, as we have demonstrated previously<sup>40</sup>. Although sulfur/composite fractions up to 79 wt% sulfur can be prepared, which corresponds to complete filling of the empty channels<sup>40</sup>, here, the sulfur/carbon ratio is optimized at a much lower level (10 wt% sulfur/composite) to provide a thin coating on the interior surfaces. An annular dark-field scanning transmission electron microscopy (STEM) image (Fig. 2a), together with energy-dispersive X-ray (EDX) carbon and sulfur maps of the same particle (Fig. 2c,d), reveal a homogeneous distribution of sulfur in the OMC-S. We conclude that sulfur is homogeneously distributed within the interior, as no sulfur 'halo' is formed on the edges of the composite particle that would be indicative of an exterior coating. An image expansion (Fig. 2a,b) on a sulfur-populated area (Fig. 2d) shows ordered channels with no contrast variation. This suggests that sulfur molecules form a thin layer on the surface of the carbon nanorods without forming aggregates that block the channels. This is in agreement with our previous studies, which indicate that sulfur wets carbon very readily<sup>40</sup>. The successful loading and ultrafine dispersion of metal and intermetallic nanoparticles into the channels of the mesoporous carbon supports the existence of the thin sulfur layer. Preservation of the long-range ordering of the channels is further confirmed by low angle X-ray diffraction (XRD; Supplementary Fig. S1a,ii).

We first sought to deposit platinum nanocrystallites to serve as proof of concept. Aqueous solutions of  $\text{H}_2\text{PtCl}_6$  were contacted with the sulfur-mediated OMC-S. For comparison, solutions of  $\text{H}_2\text{PtCl}_6$  in acetone were contacted with unmodified OMC to form 'conventional' platinum-loaded OMC<sup>24</sup>. The platinum-sorbed materials were treated in a reducing atmosphere of 7%  $\text{H}_2/\text{N}_2$ . Thermogravimetric analysis differential scanning calorimetry (TGA-DSC) measurements in air showed that sulfur is still present in the OMC-Pt composite following initial reduction to the metal at 350 °C (Supplementary Fig. S2a,b). It functions as the necessary stabilizing agent to inhibit platinum nucleation in the initial stages. The residual sulfur, which would otherwise destroy catalytic activity, is then completely removed by evacuation at 300 °C for 12 h. Its absence was determined by TGA-DSC (OMC-Pt only exhibits carbon weight loss; Supplementary Fig. S2c) and confirmed by the absence of any  $S\ [2p]$  signals in X-ray photoelectron spectra (XPS) of OMC-Pt (Fig. 3a). Samples were etched by  $\text{Ar}^+$  sputtering for 10 min to obtain XPS signals from regions within the OMC-Pt composite. Further proof of complete sulfur removal was demonstrated by the high catalytic activity of the materials (see below). The metallic nature of the platinum is also demonstrated by the characteristic platinum  $[4f]$  signal in the XPS spectra (Fig. 3b).

A significantly higher degree of platinum dispersion within channels of OMC prepared by the sulfur-entrapment route was achieved compared to the conventional wet-casting method using acetone as a solvent for impregnation<sup>24</sup>. Supplementary Fig. S1b shows the XRD pattern of conventionally prepared CMK-3/platinum composites. The reflections can be manually deconvoluted into two components. The first, highly broadened, is attributed to platinum domains 1–2 nm in size. The second sharper component arises from platinum domains with a coherence length of 6 nm, as calculated by Scherrer line broadening. This larger domain size is double that of the CMK-3 channel size, indicating that the particles are located on the external surface of the CMK-3 or their particle growth causes structural damage in the CMK-3. The poor compatibility between metal precursor solutions and carbon induces the inhomogeneity in the particle formation. In contrast, the OMC-Pt (24 wt% platinum/composite) derived from OMC-S exhibits a very narrow particle size distribution and ultrafine dispersion compared to the empty channels of OMC-S, as shown in Fig. 2e. A representative high-resolution transmission electron microscopy (HRTEM) image of these nanocrystallites is shown in Fig. 2f,

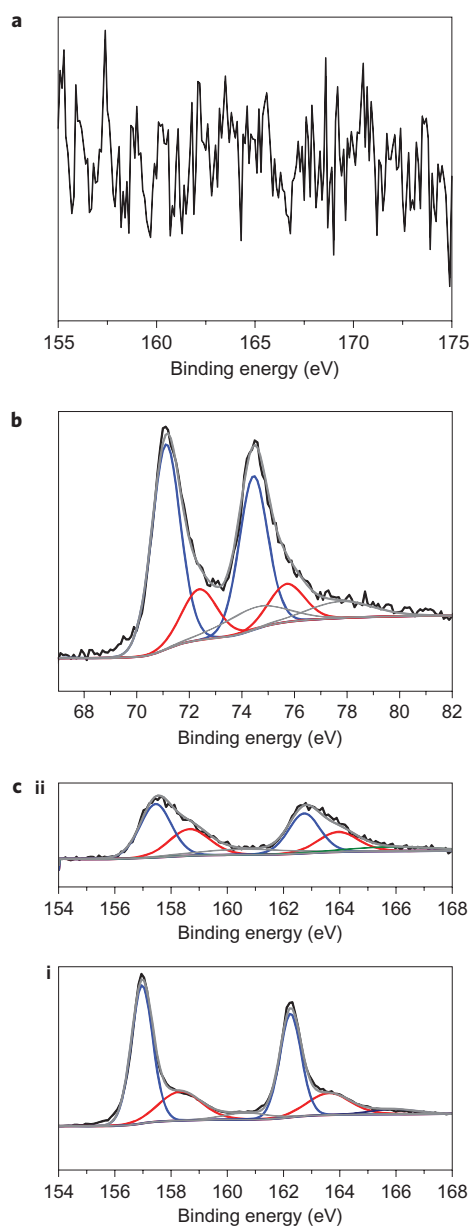


**Figure 3 | XPS spectra of platinum and PtBi nanocrystallites supported on OMC.** **a**, Sulfur  $[2p]$  signal from OMC-Pt-2 nm, demonstrating the lack of sulfur residue. **b**, Platinum  $[4f]$  signal from OMC-Pt-2 nm, with deconvolution into metallic platinum (blue trace) and  $\text{Pt-O}_x$  (surface contamination; red trace) components. **c**, Comparison of bismuth  $[4f]$  signals from bulk PtBi (i) and OMC-PtBi-3 nm (ii), showing the same high energy shift compared to metallic bismuth. The signals are deconvoluted into bismuth (blue trace) and  $\text{Bi-O}_x$  (surface contamination; red trace) components.

revealing an average diameter of 1–2 nm. These particles do not disrupt the internal carbon framework because they are smaller than the channel dimensions. The well-preserved long-range order of the carbon walls in OMC-Pt is evident in the annular dark-field STEM image (Fig. 2e) and confirmed by the sharp peaks in the low-angle XRD pattern compared to those of the OMC-S and CMK-3 (Supplementary Fig. S1a). Furthermore, the size of the platinum particles can be controlled by heat treatment up to the size of the OMC channels, that is,  $\sim 3.5$  nm. For example, platinum particles prepared at 350 °C are increased in size from less than 2 nm (OMC-Pt-1.5 nm) to  $\sim 2$  nm within 2 h under argon at 600 °C (Supplementary Fig. S3a) and to

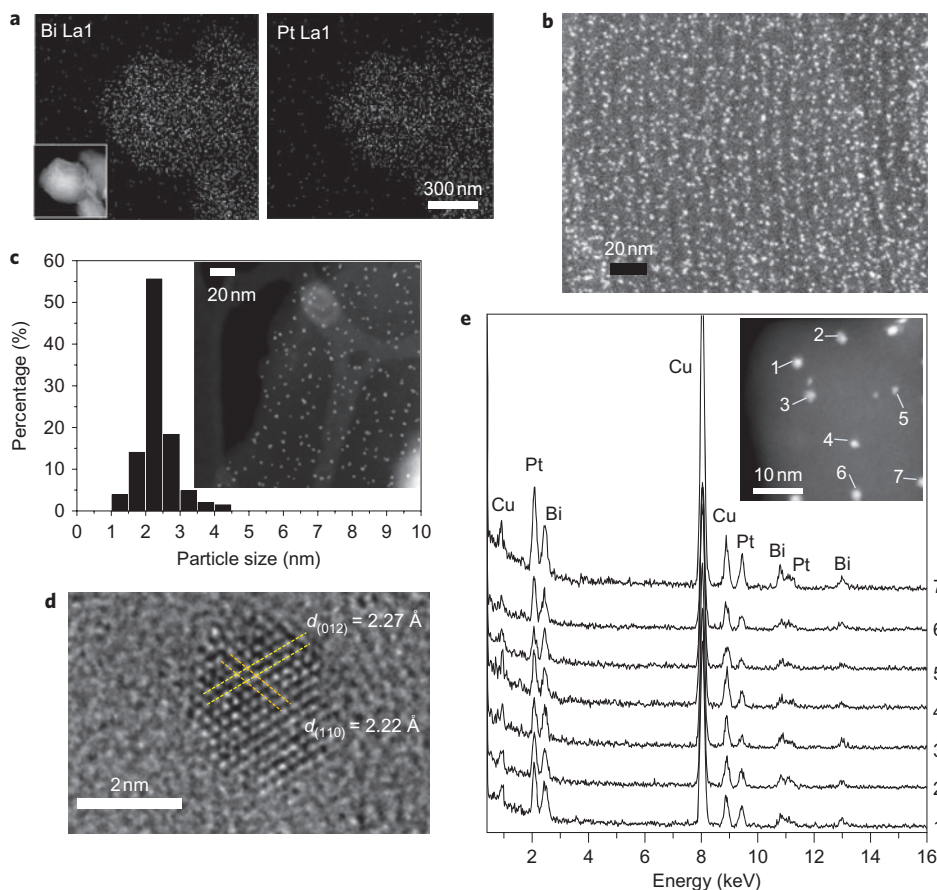


**Figure 4 | TEM images and EDX maps of OMC-PtBi, revealing homogeneously dispersed 2–3 nm crystallites of the ordered intermetallic phase.**

**a**, Platinum and bismuth EDX maps corresponding to their dark-field STEM image (inset), showing sub-nanometre mixing in the mesoporous carbon. **b**, Dark-field STEM image of OMC-PtBi-3 nm, illustrating the narrow crystallite size distribution in a representative section of the bulk. **c**, Histogram showing nanocrystallite size distribution based on a count of 407 crystallites in two different sample areas (representative STEM image shown in the inset). **d**, Bright-field HRTEM image of OMC-PtBi-3 nm, with lattice spacings marked. **e**, EDX spectra for individual PtBi nanoparticles in OMC-PtBi-3 nm; the inset shows the dark-field STEM image, with the corresponding analysed nanoparticles labelled.

~3.5 nm within 30 min at 800 °C (Supplementary Fig. S3b), as shown by HRTEM. Well-defined lattice fringes (scarcely detectable over the background intensity of the OMC for the smallest crystallites) are clearly evident in these larger crystallites (Supplementary Fig. S3).

Although the synthesis of OMC-supported platinum nanocrystallites demonstrates the viability of the methodology, our ultimate goal lies in the preparation of intermetallic or bimetallic nanocatalysts in OMC channels; at present, these cannot be realized by other methods. For many applications including formic acid oxidation for fuel cell anodes, platinum- or palladium-based intermetallic nanomaterials based on main group metals such as bismuth are of particular interest. Our route works unusually well, because it relies on the use of the OMC-S bonded platinum to act as a nucleation site for bismuth. This is akin to reports that use platinum crystals deposited on carbon to provide a growth centre for subsequent alloying with bismuth (ref. 21). The difference in our case is that the platinum clusters generated *in situ* within the carbon channels orchestrate the assembly of nearby bismuth atoms produced during reduction into an ordered intermetallic phase. In the absence of platinum, reduction of OMC-Bi(NO<sub>3</sub>)<sub>3</sub> under H<sub>2</sub>/N<sub>2</sub> at 350 °C produces bulk bismuth metal (not nano-bismuth) that forms external to the OMC-S, as shown by the XRD pattern (Supplementary Fig. S4a). This is due to the low melting temperature of bismuth (271.5 °C). Newly formed bismuth clusters agglomerate into large droplets to decrease their surface tension, unless they

can immediately form a solid phase with nearby incipient platinum clusters. A TEM image of the material heated at 350 °C for 3 h (Supplementary Fig. S5a), together with the EDX elemental maps (Fig. 4a), indicate that both platinum and bismuth are homogeneously distributed in the ordered mesoporous framework and are intimately mixed. The crystallite size was estimated roughly to be 1–2 nm from an expanded section of the image (OMC-PtBi-1.5 nm). To further crystallize the intermetallic structure (24 wt% total metal/composite), the material was heated in argon at 600 °C for 2 h. This resulted in uniform growth of the PtBi to form slightly larger, well-dispersed crystallites (Fig. 4b). A transition from PtBi-1.5 nm to larger, more ordered nanocrystallites upon heat treatment is also evident from XRD (Supplementary Fig. S1c,ii,iii), and gives rise to sharpened reflections. Although there is a considerable degree of peak broadening owing to the very small crystallite size, the reflections exhibited by OMC-PtBi-3 nm are in good agreement with that of bulk PtBi (ref. 41), and do not match that of either end member phase (platinum or bismuth) or any of their oxides. Further proof was provided by HRTEM (Fig. 4d shows a representative image of ~2.7 nm PtBi). The particles are crystalline and almost spherical in shape, as can be seen from the lattice fringes in the HRTEM. The lattice spacing and angle (~60°) of the two visible set of fringes correspond to the (012) and (110) planes of PtBi: [(012), 2.21 Å expected, 2.21 Å observed; (110), 2.15 Å expected, 2.16 Å observed; see also Supplementary Fig. S5]. These planes are unique for PtBi (Supplementary Fig. S5).

A lower-magnification STEM image and a corresponding histogram of the particle number distribution are shown in Fig. 4c. On counting  $\sim 400$  particles, the average diameter was found to be  $2.25 \pm 0.5$  nm, as shown in the histogram. We designate these OMC-PtBi-3 nm. EDX measurements were conducted on single particles from different areas of the sample using a FEI Titan STEM equipped with an aberration corrector for the electron probe and a high-brightness electron source. The EDX spectra and high-angle annular STEM image (Fig. 4e, inset) unequivocally demonstrate the existence of both platinum and bismuth (at a ratio of  $\sim 1:1$ ) in each crystallite. An additional set of spectra from a second region (Supplementary Fig. S6a) provided the same results, as did simultaneous sampling of many particles over a larger area. No Pt-Bi signal is observed in regions devoid of PtBi nanocrystallites (Supplementary Fig. S6b).

XPS spectra were also collected for composite materials. The carbon 1s signal served as an internal reference. As shown in Fig. 3c, both bulk PtBi and OMC-PtBi-3 nm exhibit a Bi  $4f_{7/2}$  signal that can be deconvoluted into two components. The minor signal at 158.4 eV is attributed to surface  $\text{Bi}_2\text{O}_3$ , formed during transfer of the sample in air to the XPS chamber (an oxide component is also apparent in the Pt 4f spectrum, Fig. 3b). The major component at 157.0–157.2 eV lies at a higher energy when compared to that of pure bismuth metal supported on OMC (156.7 eV), and is characteristic of PtBi, as reported elsewhere<sup>42</sup>. Note that nano-PtBi is also very slightly shifted to higher energy compared to bulk-PtBi.

Steady-state cyclic voltammograms (CV) of formic acid oxidation on the different catalysts, at a scan rate of  $10 \text{ mV s}^{-1}$ , are presented in Fig. 5. For OMC-Pt-2 nm, the first current maximum at 0.68 V (versus a reversible hydrogen electrode, RHE) in the anodic scan is assigned to the ‘direct path’ reaction (path 1, see above; Fig. 5a, black line). The second current maximum at 0.94 V, with a hysteresis, corresponds to oxidation of  $\text{CO}_{\text{ad}}$ , accumulated in the ‘CO path’ (path 2, see above). The ratio between the intensities of the two peaks sheds light on the question of which path is adopted more during the catalysis process. With the poisoning species consumed in the anodic scan, the current attains a higher maximum in the subsequent cathodic scan. A CV of formic acid oxidation on conventionally prepared CMK-3/platinum (that is, OMC/platinum without sulfur mediation), carried out under the same conditions, was also performed (Fig. 5a, red line). OMC-Pt-2 nm is clearly superior to CMK-3/platinum. It exhibits a lower onset potential, a higher current maximum for formic acid oxidation, and a higher peak ratio. This demonstrates that the sulfur used in catalyst preparation is fully removed and does not contaminate or poison the surface.

Figure 5b shows the voltammograms of formic acid oxidation on OMC-PtBi-1 nm and OMC-PtBi-3 nm. The catalytic performance closely resembles that of palladium/carbon catalysed formic acid oxidation, where palladium is reported to be favourable to dehydrogenation of formic acid without the formation of  $\text{CO}$ <sup>43,44</sup>. The current behaviour of formic acid oxidation in scans in both directions is nearly identical, which is a significant improvement over the pure platinum case<sup>15</sup>, or ‘large-nano’ intermetallic PtBi on carbon<sup>16</sup>. The results indicate that the dehydration path is completely eliminated for these OMC-PtBi catalysts. OMC-PtBi materials exhibit an onset potential of  $\sim 0.08$  V, which is 0.12 V lower than that of OMC-Pt-2 nm, indicating that formic acid oxidation is catalysed more easily on PtBi nanoparticles than on pure platinum. OMC-PtBi-3 nm displays superior properties to those of OMC-PtBi-1 nm by exhibiting a higher current maximum at a lower potential (0.57 V versus RHE). The improved crystallinity of the 2–3 nm PtBi particles compared with the 1 nm PtBi explains their superior properties. Furthermore, OMC-PtBi-3 nm exhibits a very high mass activity of  $770 \text{ mA mg}^{-1}$  at 0.57 V, which is double that of recently reported platinum-decorated gold nanoparticles

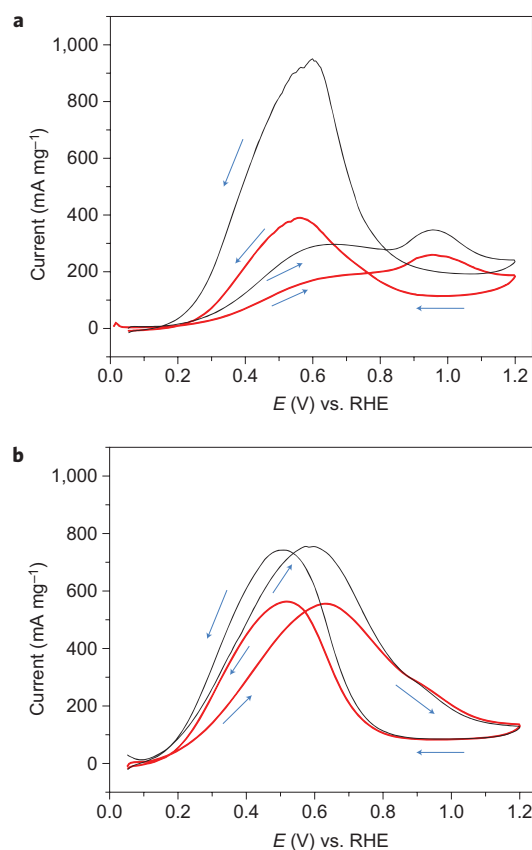


**Figure 5 | Cyclic voltammograms obtained for formic acid oxidation.**

**a**, CMK-3/platinum (red line) and OMC-Pt-2 nm (black line). **b**, OMC-PtBi-1 nm (red line) and OMC-PtBi-3 nm (black line) in 0.5 M sulfuric acid/0.5 M formic acid solution (scan rate  $10 \text{ mV s}^{-1}$ ). The electrochemical response, which is nearly identical in the forward and reverse sweeps, shows an exceptionally high mass activity.

( $400 \text{ mA mg}^{-1}$ )<sup>45</sup> and PtAg alloy nanoparticles ( $340 \text{ mA mg}^{-1}$ )<sup>46</sup> under the same conditions used here.

Chronoamperometry (CA) was carried out at a practical operating voltage of 0.3 V versus RHE to investigate the long-term stability of OMC-PtBi-3 nm. The CA curve (Supplementary Fig. S7) shows a high activity ( $800 \text{ mA mg}^{-1}$ ) with a deactivation rate of  $\sim 5\%/100$  s in the first 1,000 s. This is comparable to that of 3 nm palladium nanoparticles/OMC, which exhibits a deactivation rate of  $4.5\%/100$  s in the same time period<sup>44</sup>. At the end of the first hour, a mass activity of  $220 \text{ mA mg}^{-1}$  is achieved, and the current decay diminishes over the next 2 h to fully stabilize at  $100 \text{ mA mg}^{-1}$ . Stability tests on other bulk PtBi and PtBi nanoparticles have not been reported to our knowledge. Compared to pure platinum, which typically loses 80% of its activity in the first 60 s (ref. 47), the PtBi nano-intermetallic shows much higher mass activity and better resistivity to poisoning over the long term, as expected. When compared with state-of-the-art catalysts (for which stability data have been reported), OMC-PtBi-3 nm also exhibits good performance. It has a higher activity per gram with a similar deactivation rate when compared to  $\text{Pt}_{80}\text{Ru}_{20}$  nanoparticles<sup>48</sup> and PtPd nanoparticles<sup>17</sup>, and is comparable to that of other carbon-supported 6 nm palladium nanoparticles<sup>49</sup>. To the best of our knowledge, other than the nano-catalysts mentioned above, most either exhibit very low activity with higher stability<sup>43</sup> or suffer very fast current deactivation<sup>50</sup>. To date, simultaneously achieving high stability and very high activity remains a challenge. It not only requires highly developed synthetic techniques, but

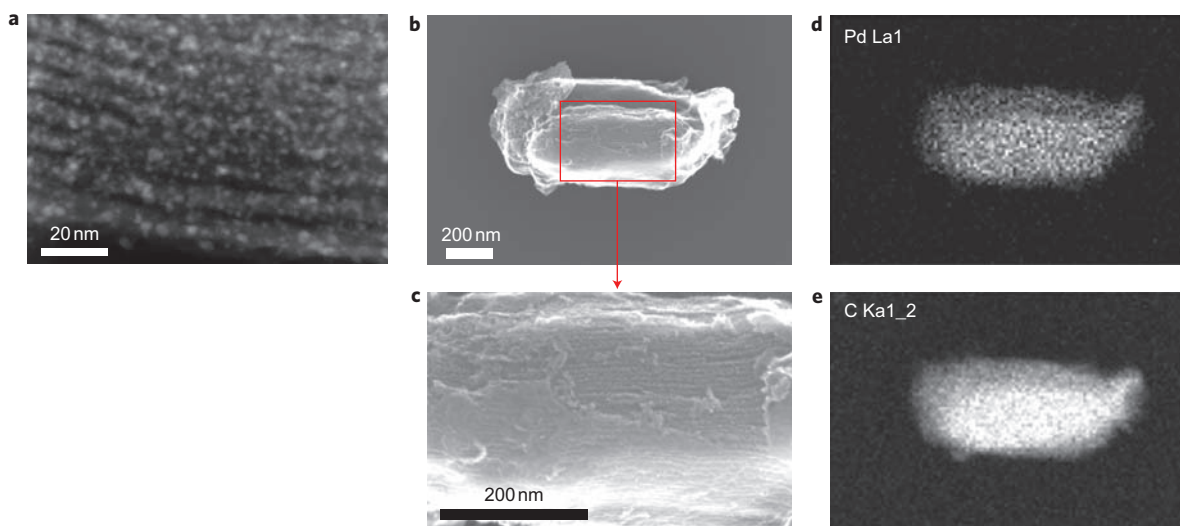


**Figure 6** | TEM and SEM images and an elemental map of nanocrystalline palladium (<3 nm) supported on OMC, prepared by the sulfur-functionalized OMC strategy. **a**, TEM image (annular dark-field STEM). **b**, SEM image. **c**, Image expansion corresponding to the area outlined by the red square in **b**. **d**, Palladium map corresponding to **b**. **e**, Carbon map corresponding to **b**.

also a more comprehensive understanding of the formic acid oxidation catalytic process.

Our preparation methodology is also widely applicable to many noble metals. With OMC-S as a support, several examples of OMC-M (12 wt% M/composite; M = Pd, Rh, Ru) were all successfully fabricated. These nanocrystalline composites also exhibit a narrow particle size distribution and a very fine dispersion on the order of  $\sim 2$  nm, as shown in their TEM images (Fig. 6a; Supplementary Figs S8d, S9d). In SEM images, these composites exhibit very clean and ordered surface morphology, indicating that the nanoparticles are well confined (Fig. 6b,c; Supplementary Figs S8a,b, S9a,b). The corresponding elemental maps of these composites identify that these metal particles are homogeneously distributed in the framework of the OMC (Fig. 6b,d,e; Supplementary Figs S8a,c, S9a,c). These materials are of interest as potential supercapacitor electrodes (ruthenium), methanol oxidation/formic acid fuel cell catalysts (palladium) or as heterogeneous catalysts for organic syntheses.

In conclusion, we describe a novel, highly effective methodology for impregnating noble metal and bimetallic nanoparticles into OMC voids with precisely controlled particle size (less than 3.5 nm in diameter) and ultrahigh dispersion. The method is applicable to a wide range of catalysts, namely bimetallic PtBi, but also metals such as Pt, Ru, Rh and Pd. OMC-supported PtBi nanocrystallites between 2 and 3.5 nm in dimension were investigated as catalysts for formic acid oxidation. They displayed the same absence of CO poisoning as bulk intermetallic phases. The larger nanocrystallites (3.5 nm) are one of the most stable catalysts reported for formic acid oxidation, and exhibit the highest level of mass activity reported for this reaction to our knowledge, under the same conditions. The excellent catalytic properties can be attributed to the successful catalyst preparation and the faithful occurrence of the ‘ensemble effect’ at the nanoscale level. Although the concept is illustrated here with nanocrystalline PtBi, the generality of this process dictates that a variety of intermetallics having at least one component that strongly interacts with sulfur could also be developed for bi- and trimetallic nanocrystallites. These can be supported on a variety of conventional and new porous carbons using this approach, with a view to use in a broad set of applications including electrocatalysis and catalysis. Ongoing work in our laboratory on other nanocrystalline PtX and trimetallic systems will be reported in forthcoming publications.

## Methods

**Synthesis of OMC-S and OMC catalysts.** CMK-3 was prepared using a nanocasting method<sup>37</sup> following the well-established procedure in the literature and with SBA-15 (ref. 43) as a hard template. Nanocomposite OMC-S was prepared following a melt-diffusion strategy<sup>40</sup>. Typically, 0.1 g of sulfur and 0.9 g of CMK-3 were ground together, and the impregnation was carried out at 155 °C. OMC-S was impregnated with catalyst precursors by dispersed it in aqueous solutions containing the desired concentration of metal precursors ( $\text{H}_2\text{PtCl}_6 \cdot 6\text{H}_2\text{O}$ , and  $\text{Pd}(\text{NO}_3)_2 \cdot 2\text{H}_2\text{O}$ ). Ethylene glycol was used to solvate precursors that easily hydrolyse in water, such as  $\text{Bi}(\text{NO}_3)_3 \cdot 5\text{H}_2\text{O}$ ,  $\text{RuCl}_3 \cdot \text{H}_2\text{O}$  and  $\text{RhCl}_3 \cdot \text{H}_2\text{O}$ . The mixture of OMC-S and precursor solution was stirred for 6 h before the solvents were evaporated. The reduction of metal precursors was completed under a flow of 7%  $\text{H}_2/\text{N}_2$  at 350 °C for 3 h. Samples were evacuated at 300 °C for 12 h to completely remove adsorbed  $\text{H}_2$  and sulfur. Higher temperatures were also used for subsequent heat treatment, as indicated in the text.

To compare the platinum loaded on OMC-S prepared by our sulfur mediation route with conventionally prepared material, 24 wt% platinum-loaded OMC was prepared using a solution of  $\text{H}_2\text{PtCl}_6$  in acetone, strictly following the literature procedure<sup>24</sup>.

For the preparation of bulk PtBi,  $\text{H}_2\text{PtCl}_6 \cdot 6\text{H}_2\text{O}$  and  $\text{Bi}(\text{NO}_3)_3 \cdot 5\text{H}_2\text{O}$  with a molar ratio of 1:1 were completely dissolved in ethylene glycol to achieve mixing at the molecular level. The solvent was then evacuated and the precursor mixture heated at 600 °C for 12 h under a flow of 7%  $\text{H}_2/\text{N}_2$ .

**Characterization.** X-ray diffraction patterns at low ( $0.75$  to  $4^\circ$  in  $2\theta$ ) and wide angle (from  $20$  to  $70^\circ$  in  $2\theta$ ) were collected on a D8-ADVANCE powder X-ray diffractometer operating at 40 kV and 30 mA and using  $\text{Cu-K}\alpha$  radiation ( $\lambda = 0.15406$  nm). The dark-field STEM was carried out with a Hitachi HD-2000 STEM. All the bright-field high-resolution TEM images and EDX spectra for individual 2–3 nm nanocrystallites based on corresponding bright-field STEM images were carried out on a FEI Titan<sup>TM</sup> 80–300 equipped with an aberration corrector for the imaging lens and monochromator and also a FEI Titan<sup>TM</sup> 80–300 Cubed equipped with a high-brightness electron source, aberration correctors of the probe-forming lens and of the imaging lens, as well as a monochromator. High-resolution imaging on the Titan 80–300 was carried out at 300 keV after tuning the aberration corrector to achieve 0.08-nm resolution in standard Young’s fringes experiments. EDX measurements on the Titan 80–300 Cubed were obtained at 80 keV to minimize electron-beam irradiation occurring due to the use the high-brightness electron source. Spectra of individual particles were collected for 300 s each while the electron beam was kept rastering on the selected individual particle so as to remove any effect of sample drift during the long acquisition time. Alignment of the system for annular dark-field imaging was carried out with the standard probe-corrector alignment procedure using gold cross-grating to achieve an imaging resolution better than 0.1 nm (ultimate information transfer better than 0.07 nm). XPS was carried out using a Thermo Scientific K-Alpha XPS spectrometer with a monochromatic Al  $\text{K}\alpha$  source (1,486.6 eV), capable of an energy resolution of 0.4–0.5 eV full-width at half-maximum.

**Electrochemical measurements.** For the preparation of working electrodes, 10.0 mg of metal/mesoporous carbon composite (24 wt% metal) was suspended in 5.0 ml of 2-propanol, and then ultrasonically blended for 30 min to form the catalyst ink.

Exactly 10  $\mu\text{l}$  of this catalyst ink was pipetted onto the surface of the glassy carbon disk electrode (geometric area of 0.196  $\text{cm}^2$ ). The catalyst-coated electrode surface was then dried under atmospheric conditions, followed by the addition of 5  $\mu\text{l}$  of 2-propanol solution containing 1 wt% Nafion, on the top of the catalyst layer. The loadings of total metals were all controlled to 24  $\mu\text{g cm}^{-2}$ .

The cell used was a conventional three-compartment electrochemical cell containing a glassy carbon (GC) disk coated with catalyst as the working electrode, platinum wire as the counter-electrode and an RHE as the reference electrode. The electrolyte was a  $\text{N}_2$ -saturated 0.5 M  $\text{H}_2\text{SO}_4$  solution containing 0.5 M HCOOH. In the CV measurements, the electrode potential was scanned in the range of 0.05–1.2 V versus RHE. Chronoamperometry was carried out with the working electrode rotating at a speed of 200 rpm to prevent fuel starvation and bubble formation on the working electrode, with its potential held at 0.3 V versus RHE, in an electrolyte solution containing 0.1 M  $\text{H}_2\text{SO}_4$ , and 0.5 M HCOOH. All the catalyst electrodes were cleaned before data collection with a steady-state CV scanned for three cycles in the range of 0.05–1.2 V versus RHE at 50  $\text{mV s}^{-1}$ . All electrochemical experiments were carried out at room temperature and ambient pressure.

Received 25 August 2009; accepted 11 January 2010;  
published online 28 February 2010

## References

- Weber, M., Wang, J. T., Wasmus, S. & Savinell, R. F. Formic acid oxidation in a polymer electrolyte fuel cell. *J. Electrochem. Soc.* **143**, L158–L160 (1996).
- Rice, C. *et al.* Direct formic acid fuel cells. *J. Power Sources* **111**, 83–89 (2002).
- Rhee, Y.-W., Ha, S. Y. & Masel, R. I. Crossover of formic acid through Nafion<sup>®</sup> membranes. *J. Power Sources* **117**, 35–38 (2003).
- Park, S., Xie, Y. & Weaver, M. J. Electrocatalytic pathways on carbon-supported platinum nanoparticles: comparison of particle-size-dependent rates of methanol, formic acid, and formaldehyde electrooxidation. *Langmuir* **18**, 5792–5798 (2002).
- Lović, J. D. *et al.* Kinetic study of formic acid oxidation on carbon-supported platinum electrocatalyst. *J. Electroanal. Chem.* **581**, 294–302 (2005).
- Capon, A. & Parsons, R. J. The oxidation of formic acid at noble metal electrodes. Part III. Intermediates and mechanism on platinum electrodes. *Electroanal. Chem.* **45**, 205–231 (1973).
- Wolter, O., Willsau, J. & Heitbaum, J. Reaction pathways of the anodic oxidation of formic acid on Pt evidenced by <sup>18</sup>O labeling—a DEMS study. *J. Electrochem. Soc.* **132**, 1635–1638 (1985).
- Sun, S. G. & Clavilier, J. The mechanism of electrocatalytic oxidation of formic acid on Pt (100) and Pt (111) in sulphuric acid solution: an emirs study. *J. Electroanal. Chem.* **240**, 147–159 (1988).
- Chang, S.-C., Ho, Y. & Weaver, M. J. Applications of real-time infrared spectroscopy to electrocatalysis at bimetallic surfaces: I. Electrooxidation of formic acid and methanol on bismuth-modified Pt(111) and Pt(100). *Surf. Sci.* **265**, 81–94 (1992).
- Llorca, M. J., Herrero, E., Feliu, J. M. & Aldaz, A. Formic acid oxidation on Pt(111) electrodes modified by irreversibly adsorbed selenium. *J. Electroanal. Chem.* **373**, 217–225 (1994).
- Leiva, E., Iwasita, T., Herrero, E. & Feliu, J. M. Effect of adatoms in the electrocatalysis of HCOOH oxidation. A theoretical model. *Langmuir* **13**, 6287–6293 (1997).
- Smith, S. P. E. & Abruña, H. D. Structural effects on the oxidation of HCOOH by bismuth modified Pt(111) electrodes with (110) monatomic steps. *J. Electroanal. Chem.* **467**, 43–49 (1999).
- Schmidt, T. J. & Behm, R. J. Formic acid oxidation on pure and Bi-modified Pt(111): temperature effects. *Langmuir* **16**, 8159–8166 (2000).
- Spendelov, J. S. & Wieckowski, A. Noble metal decoration of single crystal platinum surfaces to create well-defined bimetallic electrocatalysts. *Phys. Chem. Chem. Phys.* **6**, 5094–5118 (2004).
- Casado-Rivera, E. *et al.* Electrocatalytic oxidation of formic acid at an ordered intermetallic PtBi surface. *ChemPhysChem.* **4**, 193–199 (2003).
- Casado-Rivera, E. *et al.* Electrocatalytic activity of ordered intermetallic phases for fuel cell applications. *J. Am. Chem. Soc.* **126**, 4043–4049 (2004).
- Rice, C., Ha, S., Masel, R. I. & Wieckowski, A. Catalysts for direct formic acid fuel cells. *J. Power Sources* **115**, 229–235 (2003).
- Roychowdhury, C., Matsumoto, F., Mutolo, P. F., Abruña, H. D. & DiSalvo, F. J. Synthesis, characterization, and electrocatalytic activity of PtBi nanoparticles prepared by the polyol process. *Chem. Mater.* **17**, 5871–5876 (2005).
- Roychowdhury, C. *et al.* Synthesis, characterization, and electrocatalytic activity of PtBi and PtPb nanoparticles prepared by borohydride reduction in methanol. *Chem. Mater.* **18**, 3365–3372 (2006).
- Matsumoto, F., Roychowdhury, C., DiSalvo, F. J. & Abruña, H. D. Electrocatalytic activity of ordered intermetallic PtPb nanoparticles prepared by borohydride reduction toward formic acid oxidation. *J. Electrochem. Soc.* **155**, B148–B154 (2008).
- Bauer, J. C., Chen, X., Liu, Q., Phan, T.-H. & Schaak, R. E. Converting nanocrystalline metals into alloys and intermetallic compounds for applications in catalysis. *J. Mater. Chem.* **18**, 275–282 (2008).
- Chan, K.-Y., Ding, J., Ren, J., Cheng, S. & Tsang, K. Y. Supported mixed metal nanoparticles as electrocatalysts in low temperature fuel cells. *J. Mater. Chem.* **14**, 505–516 (2004).
- Ryoo, R., Joo, S. H. & Jun, S. Synthesis of highly ordered carbon molecular sieves via template-mediated structural transformation. *J. Phys. Chem. B* **103**, 7743–7746 (1999).
- Joo, S. *et al.* Ordered nanoporous arrays of carbon supporting high dispersions of platinum nanoparticles. *Nature* **412**, 169–172 (2001).
- Joo, J. B., Kim, P., Kim, W., Kim, J. & Yi, J. Preparation of mesoporous carbon templated by silica particles for use as a catalyst support in polymer electrolyte membrane fuel cells. *Catal. Today* **111**, 171–175 (2006).
- Nam, J.-H., Jang, Y.-Y., Kwon, Y.-U. & Nam, J.-D. Direct methanol fuel cell Pt-carbon catalysts by using SBA-15 nanoporous templates. *Electrochem. Commun.* **6**, 737–741 (2004).
- Yu, J.-S., Kang, S., Yoon, S. B. & Chai, G. Fabrication of ordered uniform porous carbon networks and their application to a catalyst supporter. *J. Am. Chem. Soc.* **124**, 9382–9383 (2002).
- Liu, H. *et al.* A review of anode catalysis in the direct methanol fuel cell. *J. Power Sources* **155**, 95–110 (2006).
- Li, Z., Yan, W. & Dai, S. Surface functionalization of ordered mesoporous carbons—a comparative study. *Langmuir* **21**, 11999–12006 (2005).
- Guo, Z. *et al.* Adsorption of vitamin B12 on ordered mesoporous carbons coated with PMMA. *Carbon* **43**, 2344–2351 (2005).
- Calvillo, L. *et al.* Platinum supported on functionalized ordered mesoporous carbon as electrocatalyst for direct methanol fuel cells. *J. Power Sources* **169**, 59–64 (2007).
- Choi, W. *et al.* Platinum nanoclusters studded in the microporous nanowalls of ordered mesoporous carbon. *Adv. Mater.* **17**, 446–451 (2005).
- Wen, Z., Liu, J. & Li, J. Core/shell Pt/C nanoparticles embedded in mesoporous carbon as a methanol-tolerant cathode catalyst in direct methanol fuel cells. *Adv. Mater.* **20**, 743–747 (2008).
- Liu, S. *et al.* Fabrication and characterization of well-dispersed and highly stable PtRu nanoparticles on carbon mesoporous material for applications in direct methanol fuel cell. *Chem. Mater.* **20**, 1622–1628 (2008).
- Orilall, M. C. *et al.* One-pot synthesis of platinum-based nanoparticles incorporated into mesoporous niobium oxide-carbon composites for fuel cell electrodes. *J. Am. Chem. Soc.* **131**, 9389–9395 (2009).
- Zhu, Y., Kockrick, E., Kaskel, S., Ikoma, T. & Hanagata, N. Nanocasting route to ordered mesoporous carbon with FePt nanoparticles and its phenol adsorption property. *J. Phys. Chem. C* **113**, 5998–6002 (2009).
- Jun, S. *et al.* Synthesis of new, nanoporous carbon with hexagonally ordered mesostructure. *J. Am. Chem. Soc.* **122**, 10712–10713 (2000).
- Chen, I. Molecular-orbital studies of charge carrier transport in orthorhombic sulfur. I. Molecular orbitals of S<sub>8</sub>. *Phys. Rev. B* **2**, 1053–1060 (1970).
- Miller, J. T. & Koningsberger, D. C. The origin of sulfur tolerance in supported platinum catalysts: the relationship between structural and catalytic properties in acidic and alkaline Pt/LTL. *J. Catal.* **162**, 209–219 (1996).
- Ji, X., Lee, K. T. & Nazar, L. F. A highly ordered nanostructured carbon-sulphur cathode for lithium-sulphur batteries. *Nat. Mater.* **8**, 500–506 (2009).
- Zhuravlev, N. N. & Stepanova, A. A. An X-ray investigation of superconducting alloys of bismuth with platinum in the range of 20–640 °C. *Sov. Phys.-Crystallogr.* **7**, 231–242 (1962).
- Blasini, D. R. *et al.* Surface composition of ordered intermetallic compounds PtBi and PtPb. *Surf. Sci.* **600**, 2670–2680 (2006).
- Zhou, W. P. *et al.* Size effects in electronic and catalytic properties of unsupported palladium nanoparticles in electrooxidation of formic acid. *J. Phys. Chem. B* **110**, 13393–13398 (2006).
- Ge, J. *et al.* Controllable synthesis of Pd nanocatalysts for direct formic acid fuel cell (DFAFC) application: from Pd hollow nanospheres to Pd nanoparticles. *J. Phys. Chem. C* **111**, 17305–17310 (2007).
- Kristian, N., Yanb, Y. & Wang, X. Highly efficient submonolayer Pt-decorated Au nano-catalysts for formic acid oxidation. *Chem. Commun.* 353–355 (2008).
- Xu, J. B., Zhao, T. S. & Liang, Z. X. Synthesis of active platinum-silver alloy electrocatalyst toward the formic acid oxidation reaction. *J. Phys. Chem. C* **112**, 7362–7368 (2008).
- Tian, N., Zhou, Z., Sun, S., Ding, Y. & Wang, Z. Synthesis of tetrahedral platinum nanocrystals with high-index facets and high electro-oxidation activity. *Science* **316**, 732–735 (2007).
- Rigsby, M. A. *et al.* Experiment and theory of fuel cell catalysis: methanol and formic acid decomposition on nanoparticle Pt/Ru. *J. Phys. Chem. C* **112**, 15595–15601 (2008).
- Huang, Y. *et al.* Preparation of Pd/C catalyst for formic acid oxidation using a novel colloid method. *Electrochem. Commun.* **10**, 621–624 (2008).
- Yu, X. & Pickup, P. G. Recent advances in direct formic acid fuel cells (DFAFC). *J. Power Sources* **182**, 124–132 (2008).

### Acknowledgements

L.F.N. gratefully acknowledges the financial support of the National Science and Engineering Research Council (NSERC, Canada) through its Discovery Grant and Canada Research Chair programs. We thank R. Sodhi at Surface Interface Ontario, University of Toronto, for acquisition and processing of the XPS spectra and C. Mims for helpful discussions, N. Coombs at the Centre for Nanostructured Imaging, University of Toronto, for help with acquisition of the STEM imaging, and C. Andrei (McMaster University, Canadian Centre for Electron Microscopy) for help with the high-resolution imaging work. The experimental work on the FEI Titan 80–300 and FEI Titan 80–300 Cubed was carried out at the Canadian Centre for Electron Microscopy, a user facility supported by NSERC and McMaster University.

### Author contributions

X.J. and L.N. designed and conducted the research. Electrochemical experiments were performed by X.J., L.Z., and J.Z. K.L. and R.H. contributed analysis. TEM experiments were performed by G.B. and M.C. L.N. and X.J. wrote the paper.

### Additional information

The authors declare no competing financial interests. Supplementary information accompanies this paper at [www.nature.com/naturechemistry](http://www.nature.com/naturechemistry). Reprints and permission information is available online at <http://npg.nature.com/reprintsandpermissions/>. Correspondence and requests for materials should be addressed to L.F.N.